U01HG004279 (D.M.M.), U01HG004261 (E.L.), U01HG004274 (S.H.), and U41HG004269 (L.S.). Awards to S.E.C. and G.H.K. were carried out at LBNL under contract no. DE-AC02-05CH11231. Additional support was provided by the NSF under grant 0937060 to the Computing Research Association for the CIFellows Project (S.R.) and under award no. 0905968 (J.E.), a Natural Sciences and Engineering Research Council of Canada (NSERC) fellowship (B.A.), T. Kahveci (F.A.), the Japan Society for the Promotion of Science (K.O.), the Swedish Research Council (Q.D.), a NIH National Research Service Award postdoctoral fellowship (C.A.B.), a National Defense Science and Engineering Graduate Fellowship (R.S.), an Erwin Schrödinger Fellowship of the Austrian Fonds zur Förderung der wissenschaftlichen Forschung (S.W.), a Leukemia and Lymphoma Society fellowship (S.W.), a Lilly-Life Sciences Research Foundation fellowship (C.D.B.), a NSERC postdoctoral fellowship (C.G.A.), Affymetrix (T.G.R.), a fellowship from the Swiss National Science Foundation (D.M.), a German Research Foundation grant WI 3628/1-1 (S.W.), a HHMI Damon Runyon Cancer Research fellowship (J.T.N.), the Indiana Genomics Initiative (T.C.K.), H. Smith and the NIDDK genomics core laboratory (B.O.), NIH R01HG004037, NSF CAREER award 0644282, and the Sloan Foundation (M.K.). A full list of author contributions is available in the SOM.

Complete Author List

Kellis (integration): Sushmita Roy, Jason Ernst, Pouya Kheradpour, Christopher A. Bristow, Michael F. Lin, Stefan Washietl, Ferhat Ay, Patrick E. Meyer, Luisa Di Stefano, Rogerio Candeias, Irwin Jungreis, Daniel Marbach, Rachel Sealfon, Manolis Kellis
Celniker (transcription): Jane M. Landolin, Joseph W. Carlson, Benjamin Booth, Angela N. Brooks, Carrie A. Davis, Michael O. Duff, Philipp Kapranov, Anastasia A. Samsonova, Jeremy E. Sandler, Marijke J. van Baren, Kenneth H. Wan, Li Yang, Charles Yu, Justen Andrews, Steven E. Brenner, Michael R. Brent, Lucy Cherbas, Thomas R. Gingeras, Roger A. Hoskins, Thomas C. Kaufman, Norbert Perrimon, Peter Cherbas, Brenton R. Graveley, Susan E. Celniker, Charles L. G. Comstock, Alex Dobin, Jorg Drenkow, Sandrine Dudoit, Jacqueline Dumais, Delphine Fagegaltier, Srinka Ghosh, Kasper D. Hansen, Sonali Jha, Laura Langton, Wei Lin, David Miller, Aaron E. Tenney, Huaien Wang, Aarron T. Willingham, Chris Zaleski, Dayu Zhang
Karpen (chromatin): Peter V. Kharchenko, Michael Y. Tolstorukov, Artyom A. Alekseyenko, Andrey A. Gorchakov, Tingting Gu, Aki Minoda, Nicole C. Riddle, Yuri B. Schwartz, Sarah C. R. Elgin, Mitzi I. Kuroda, Vincenzo Pirrotta, Peter J. Park, Gary H. Karpen, David Acevedo, Eric P. Bishop, Sarah E. Gadel, Youngsook L. Jung, Cameron D. Kennedy, Ok-Kyung Lee, Daniela Linder-Basso, Sarah E. Marchetti, Gregory Shanower
White (transcription factors): Nicolas Nègre, Lijia Ma, Christopher D. Brown, Rebecca Spokony, Robert L. Grossman, James W. Posakony, Bing Ren, Steven Russell, Kevin P. White, Richard Auburn, Hugo J. Bellen, Jia Chen, Marc H. Domanus, David Hanley, Elizabeth Heinz, Zirong Li, Folker Meyer, Steven W. Miller, Carolyn A. Morrison, Douglas A. Scheftner, Lionel Senderowicz, Parantu K. Shah, Sarah Suchy, Feng Tian, Koen J. T. Venken, Robert White, Jared Wilkening, Jennifer Zieba
MacAlpine (replication): Matthew L. Eaton, Heather K. MacAlpine, Jared T. Nordman, Sara K. Powell, Noa Sher, Terry L. Orr-Weaver, David M. MacAlpine, Leyna C. DeNapoli, Queying Ding, Thomas Eng, Helena Kashevsky, Sharon Li, Joseph A. Prinz
Lai (small RNAs): Nicolas Robine, Eugene Berezikov, Qi Dai, Katsutomo Okamura, Eric C. Lai, Qi Dai, Gregory J. Hannon, Martin Hirst, Marco Marra, Michelle Rooks, Yongjun Zhao
Henikoff (nucleosomes): Jorja G. Henikoff, Akiko Sakai, Kami Ahmad, Steven Henikoff, Terri D. Bryson
Stein (data coordination center): Bradley I. Arshinoff, Nicole L. Washington, Adrian Carr, Xin Feng, Marc D. Perry, William J. Kent, Suzanna E. Lewis, Gos Micklem, Lincoln D. Stein, Galt Barber, Aurelien Chateigner, Hiram Clawson, Sergio Contrino, Francois Guillier, Angie S. Hinrichs, Ellen T. Kephart, Paul Lloyd, Rachel Lyne, Sheldon McKay, Richard A. Moore, Chris Mungall, Kim M. Rutherford, Peter Ruzanov, Richard Smith, E. O. Stinson, Zheng Zha
Oliver (comparative transcription): Carlo G. Artieri, Renhua Li, John H. Malone, David Sturgill, Brian Oliver, Lichun Jiang, Nicolas Mattiuzzo
RNA structure: Sebastian Will, Bonnie Berger
Program management: Elise A. Feingold, Peter J. Good, Mark S. Guyer, Rebecca F. Lowdon

Supporting Online Material

www.sciencemag.org/cgi/content/full/science.1198374/DC1
Materials and Methods
SOM Text
Figs. S1 to S23
Tables S1 to S7
Data Sets S1 to S17 (available at www.modencode.org/publications/integrative_fly_2010/)

28 September 2010; accepted 30 November 2010
Published online 22 December 2010;
10.1126/science.1198374

Downloaded from www.sciencemag.org on January 3, 2011

High-Flux Solar-Driven Thermochemical Dissociation of CO_2 and H_2O Using Nonstoichiometric Ceria

William C. Chueh,[1] Christoph Falter,[2] Mandy Abbott,[1] Danien Scipio,[1] Philipp Furler,[2] Sossina M. Haile,[1]* Aldo Steinfeld[2,3]*

Because solar energy is available in large excess relative to current rates of energy consumption, effective conversion of this renewable yet intermittent resource into a transportable and dispatchable chemical fuel may ensure the goal of a sustainable energy future. However, low conversion efficiencies, particularly with CO_2 reduction, as well as utilization of precious materials have limited the practical generation of solar fuels. By using a solar cavity-receiver reactor, we combined the oxygen uptake and release capacity of cerium oxide and facile catalysis at elevated temperatures to thermochemically dissociate CO_2 and H_2O, yielding CO and H_2, respectively. Stable and rapid generation of fuel was demonstrated over 500 cycles. Solar-to-fuel efficiencies of 0.7 to 0.8% were achieved and shown to be largely limited by the system scale and design rather than by chemistry.

Long-term storage and long-range transport of the vast, yet intermittent and unevenly distributed, solar energy resource is essential for a transition away from fossil energy (*1*). Chemical fuels, derived from CO_2 and/or H_2O, offer exceptional energy density and convenience for transportation, but their production using solar energy input has remained a grand challenge (*2*–*9*). Solar-driven thermochemical approaches to CO_2 and H_2O dissociation inherently operate at high temperatures and use the entire solar spectrum; as such, they provide an attractive path to solar fuel production at high rates and efficiencies in the absence of precious metal catalysts (*10*). In contrast to direct thermolysis of CO_2 and H_2O, two-step thermochemical cycles using metal oxide redox reactions further bypass the CO-O_2 or H_2-O_2 separation problem (*11*). Among candidate redox materials, ferrite-based oxides exhibit relatively slow reaction rates, degradation in rates because of sintering, and losses because of uncontrolled volatilization, whereas ZnO, SnO_2, and analogous volatile oxides that sublime during decomposition require rapid quenching of gaseous products to avoid recombination (*10*–*18*). Cerium oxide (ceria) has emerged as a highly attractive redox active material choice for two-step thermochemical cycling because it displays rapid fuel production kinetics and high selectivity (*17*, *19*–*24*), where such features result, in part, from the absence of distinct oxidized and reduced phases. However, ceria-based thermochemical studies to date have largely been limited to bench-top demonstrations of components or individual steps of the solar fuel production cycle; assessment of cyclability has been limited, and the energy conversion efficiency has remained uncertain because of the relatively low gravimetric fuel productivity inherent to the nonstoichiometric process. Here, we demonstrate high-rate solar fuel production from both CO_2 and H_2O using a solar reactor subjected directly to concentrated radiation under realistic operating conditions relevant to large-scale industrial implementation, without the need for complex material microstructures and/or system design (e.g., additional quench or separation steps). The results provide compelling evidence for the viability of thermochemical approaches to solar fuel

[1]Materials Science, California Institute of Technology, MC 309-81, Pasadena, CA 91125, USA. [2]Department of Mechanical and Process Engineering, Eidgenössische Technische Hochschule (ETH) Zürich, 8092 Zürich, Switzerland. [3]Solar Technology Laboratory, Paul Scherrer Institute, 5232 Villigen PSI, Switzerland.

*To whom correspondence should be addressed. E-mail: smhaile@caltech.edu (S.M.H.); aldo.steinfeld@ethz.ch (A.S.)

generation while clarifying the efforts required to transform the concept into a central technology in a sustainable energy future.

Thermochemical H_2O-CO_2-splitting cycles over a nonstoichiometric oxide are described by the following pairs of reactions:

Higher temperature, T_H

$$^1/_\delta MO_2 \rightarrow {}^1/_\delta MO_{2-\delta} + {}^1/_2 O_2(g) \quad (1)$$

Lower temperature, T_L

$$H_2O(g) + {}^1/_\delta MO_{2-\delta} \rightarrow {}^1/_\delta MO_2 + H_2(g) \quad (2a)$$

Lower temperature, T_L

$$CO_2(g) + {}^1/_\delta MO_{2-\delta} \rightarrow {}^1/_\delta MO_2 + CO(g) \quad (2b)$$

Net H_2O dissociation

$$H_2O(g) \rightarrow {}^1/_2 O_2(g) + H_2(g) \quad (3a)$$

Net CO_2 dissociation

$$CO_2(g) \rightarrow {}^1/_2 O_2(g) + CO(g) \quad (3b)$$

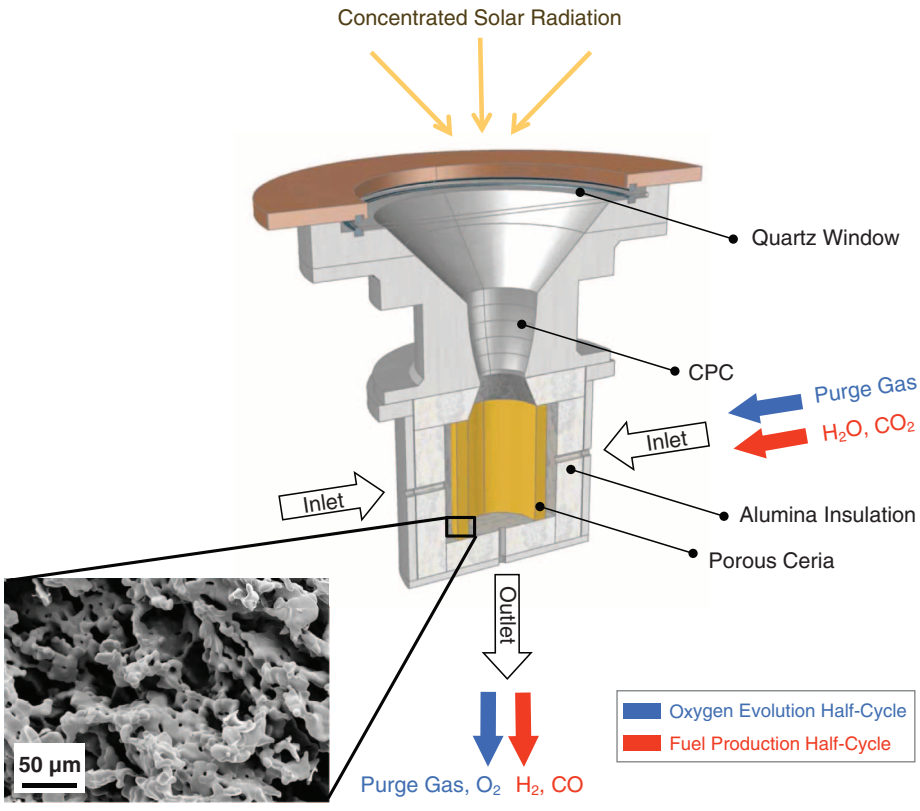

Fig. 1. Schematic of the solar reactor for the two-step, solar-driven thermochemical production of fuels. It consists of a thermally insulated cavity receiver containing a porous monolithic ceria cylinder. Concentrated solar radiation enters through a windowed aperture and impinges on the ceria inner walls. Reacting gases flow radially across the porous ceria toward the cavity inside, whereas product gases exit the cavity through an axial outlet port at the bottom. (**Inset**) The scanning electron micrograph of the porous ceria tube after 23 cycles. Blue arrows indicate ceria reduction (Eq. 1); red arrows indicate oxidation (Eqs. 2a and 2b).

where M in the present case is Ce or a combination of Ce and a dopant element. At the relatively high temperatures of the present study (>800°C), equilibria of reaction (2b) involving carbonaceous species can be neglected (*21*).

The solar reactor constructed for the purposes of demonstrating these cycles is schematically shown in Fig. 1. It consists of a cavity receiver with a windowed aperture through which concentrated solar radiation enters. The selected dimensions ensure multiple internal reflections and efficient capture of incoming solar energy; the apparent absorptivity exceeds 0.94, approaching the ideal blackbody limit (*25*). Porous, monolithic ceria, assembled from quarter-circular-arc pieces in the form of a cylinder (325 g in mass, 35 mm in outer diameter, 102 mm in height, and 80% in porosity as fabricated), is placed inside the cavity and subjected to multiple heat-cool cycles under appropriate gases to induce fuel production (Fig. 2). No additional support or absorber was used.

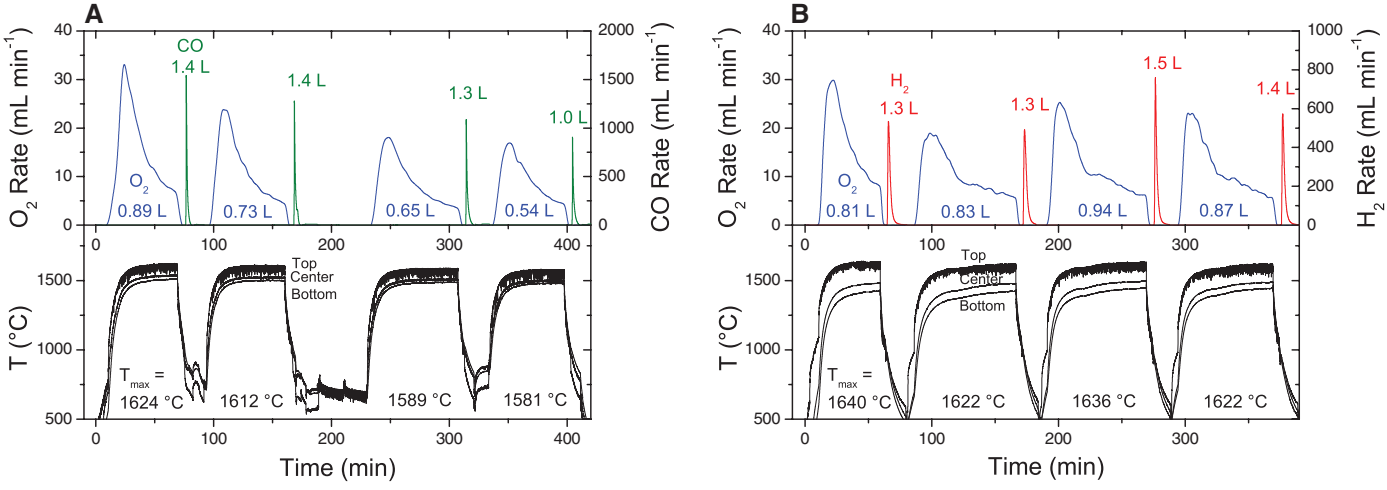

Fig. 2. Thermochemical cycling of ceria (325 g) using the solar reactor with (**A**) CO_2 and (**B**) H_2O as oxidant. The oxygen and fuel evolution rates as well as the total volume of gas evolved are shown. Temperatures were measured at three positions along the height of the ceria tube. Maximum temperatures (T_{max}) attained in the reactor are shown. Conditions for (A) were as follows: Ar sweep gas at a flow rate of 0.0062 liter min^{-1} g^{-1} of ceria during the ceria reduction half-cycle, and CO_2/Ar at p_{CO_2} = 0.78 atm and a flow rate of 0.035 liter min^{-1} g^{-1} of ceria during the ceria oxidation half-cycle. Conditions for (B) were as follows: Ar sweep gas at a flow rate of 0.023 liter min^{-1} g^{-1} of ceria during the ceria reduction half-cycle, and H_2O/Ar at p_{H_2O} = 0.78 atm and a flow rate of 0.035 liter min^{-1} g^{-1} of ceria during the ceria oxidation half-cycle.

Downloaded from www.sciencemag.org on January 3, 2011

With this arrangement, the porous ceria cylinder is directly exposed to concentrated solar radiation impinging on its inner walls. An annular gap between the ceria cylinder and the alumina insulation tiles suppresses undesired reactions between the two components. Reacting gases are injected into this annular gap and directed to flow radially across the porous ceria cylinder toward the cavity inside, whereas product gases exit the cavity through an axial outlet port at the bottom. Complete experimental details, including procedures for estimating uncertainty, are given in (*25*). Post situ x-ray diffraction showed that, with the exception of the portion in direct contact with the insulation material, the ceria remained phase-pure and free of detectable alumina incorporation (fig. S1).

To drive oxygen evolution (Eq. 1), we purged the solar reactor with flowing argon [partial pressure of O_2 (p_{O_2}) = 10^{-5} atm] and ramped the incident radiation power to about 1.9 kW at a mean solar flux intensity over the aperture of 1500 suns (1 sun = 1 kW m^{-2}), typical of a commercial solar dish or a tower concentration system. The temperature of the ceria tube rose to values between 1420° and 1640°C, with the exact temperature dependent on the position within the reactor and on the cycle (Fig. 2A). The rise in temperature was rapid below 1250°C, averaging 140°C min^{-1}, but slowed to about 8°C min^{-1} as the temperature approached a steady-state value because of increasing heat dissipation by re-radiation through the aperture and conduction heat transfer through the insulation. Oxygen evolution from ceria was observed at an onset temperature of about 900°C, consistent with equilibrium thermogravimetry measurements (fig. S2). The rate of evolution increased with temperature, reaching a peak value of 34 ± 2 ml min^{-1} (STP, standard temperature and pressure) and an average value of 16 ± 1 ml min^{-1} (averaged over the time required to reach 90% of the extent of reaction) on the first cycle (Fig. 2A). When the rate dropped to 20% of the peak value, the evolution reaction was terminated by decreasing the intensity of the incident radiation flux. Upon cooling to ~900°C, CO_2 was injected into the solar reactor. Production of CO was immediately observed, reaching a remarkable peak rate of $1.5 \times 10^3 \pm 0.1 \times 10^3$ ml min^{-1} (STP) and an average rate of $5.9 \times 10^2 \pm 0.4 \times 10^2$ ml min^{-1} (STP) (Fig. 2A). Consistent with the fact that there was no water present in the reactant stream, no gas-phase C_1, C_2, or C_3 hydrocarbons were detected by the gas chromatograph. Carbon-neutral balance (<3% C unaccounted for, well within error) was achieved by summing the flow rates of CO_2 in the reactant stream and CO_2 and CO in the product steam. As verification, temperature-programmed oxidation was performed on the ceria after the CO_2 dissociation reaction by flowing oxygen into the solar reactor while ramping the temperature to 1000°C (*26*). Both CO and CO_2 levels were below the detection limit, confirming that no appreciable amount of carbonaceous species was deposited onto ceria during CO_2 dissociation and that a 100% selectivity toward CO production was achieved. Upon the termination of CO production, the radiation flux was increased and the entire cycle repeated. A slight decline over the four cycles in the nominal reactor temperature attained during the O_2 release step (from 1624° to 1581°C) is responsible for the observed slight decline in O_2 release and CO yield. An analogous set of experiments was also performed for H_2O dissociation, with H_2 production rate reaching a peak value of $7.6 \times 10^2 \pm 0.8 \times 10^2$ ml min^{-1} (STP) and a maximum average value of $3.1 \times 10^2 \pm 0.3 \times 10^2$ ml min^{-1} (STP) (Fig. 2B). A total of 23 cycles were performed. An experimental run performed without the ceria confirmed the absence of O_2, CO, or H_2 evolution under corresponding reaction conditions.

The characteristics of solar-thermochemical fuel production from ceria reveal several important features of the cycling process. Although the behavior is generally reproducible between cycles, some run-to-run variations are evident. The oxygen evolution reaches a peak value between 17 and 34 ml min^{-1}, whereas the total amount evolved ranges from 0.54 to 0.94 liter for 325 g of ceria. As noted, these differences are correlated with the peak reactor temperature obtained (Fig. 2), variations in which are attributed to unsteady heat transfer. Taking this temperature variability into account, the total oxygen evolution is found to be generally consistent with thermodynamic expectations (fig. S2). Mass balance considerations further dictate a 2-to-1 molar (and hence volumetric) ratio of fuel produced to oxygen released for full utilization of the ceria nonstoichiometry. For CO_2 dissociation, the CO:O_2 ratio ranged from 1.6 ± 0.2:1 to 2.0 ± 0.2:1, whereas for H_2O dissociation, the H_2:O_2 ratio was 1.6 ± 0.2:1. The slight deviation from the ideal value is attributed to small leaks in the system and to the accuracies of the electronic mass flow controller and measured gas composition.

Perhaps the most obvious feature of the cycling behavior in Fig. 2 is the much faster rate of fuel production than that of O_2 release. It was observed that lowering the purge gas flow rate during ceria reduction by a factor of 4 had negligible impact on the oxygen evolution rate (Fig. 2), indicating that the convective transport of oxygen gas in the reactor is not likely the rate-limiting step. Furthermore, the substantial difference in the O_2 evolution and CO_2 dissociation rate suggests that gas-phase transport through the pores of ceria is probably not rate-limiting. We considered, as an alternative, that the oxygen evolution kinetics in the solar reactor are

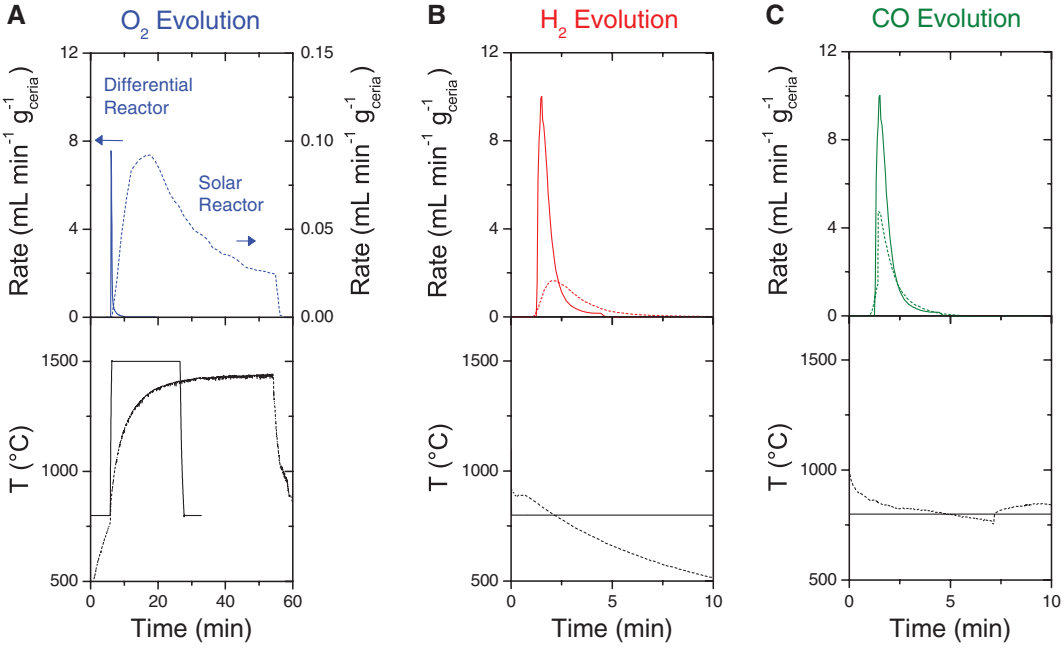

Fig. 3. Comparison of (**A**) O_2, (**B**) H_2, and (**C**) CO evolution between the solar reactor (dotted lines) and the differential reactor (solid lines). Experimental conditions for the solar reactor are the same as those for Fig. 2. In the differential reactor, 0.429 g of CeO_2 was cycled between 1500°C (Ar sweep gas flow rate = 2.3 liter min^{-1} g^{-1} of ceria, 20 min) and 800°C (for CO_2 splitting, p_{CO_2} = 0.50 atm, flow rate = 1.2 liter min^{-1} g^{-1} of ceria, 10 min; for H_2O splitting, p_{H_2O} = 0.44 to 0.52 atm, flow rate = 2.1 to 2.5 liter min^{-1} g^{-1} of ceria, 10 min).

Downloaded from www.sciencemag.org on January 3, 2011

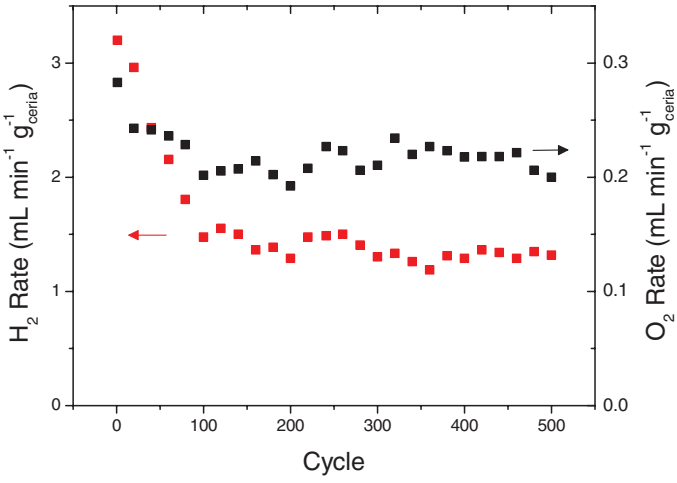

Fig. 4. O_2 (black) and H_2 (red) evolution rates for 500 water-splitting cycles. CeO_2 was cycled between 1500°C (p_{O_2} =10^{-5} atm, flow rate = 3.2 liter min^{-1} g^{-1} of ceria, 10 min, ramp rate = 100°C min^{-1}) and 800°C (p_{H_2O} = 0.13 to 0.15 atm, flow rate = 0.75 to 0.76 liter min^{-1} g^{-1} of ceria, 10 min). The gas evolution rate is calculated by averaging the instantaneous rate over the time required to reach 90% of the gas produced.

limited by the heating rate, a factor that does not affect fuel production because this step occurs isothermally. If the heating rate is slow relative to the surface reaction and solid-state diffusion steps involved in oxygen release, we can express the oxygen evolution rate as $d\delta/dt \approx (d\delta/dT)_{T=T(t)}(dT/dt)$, where δ is ceria oxygen nonstoichiometry (Eq. 1), T is temperature, and t is time. By using the spatially averaged temperature profile in the first cycle in Fig. 2A, we compute a maximum oxygen evolution rate of 65 ml min^{-1}, which, given the approximate nature of the calculation, is comparable to the observed rate.

To eliminate the effect of gas-phase mass and heat transfer, we carried out thermochemical cycling of ceria by using identically prepared monolithic porous samples (annealed for 50 hours to simulate cycling conditions) in a smaller-scale infrared imaging furnace that uses only a 0.4-g sample. Such an experimental setup permitted thermochemical cycling under high-flow, differential reactor conditions, in which the sample temperature could be changed rapidly (average ramp rate of 1700°C min^{-1}) and the gas composition approached uniformity. Under these ideal conditions in which only surface chemical reactions and solid-state oxygen diffusion in ceria limit the overall reaction rate, oxygen evolution (Fig. 3) attained a peak instantaneous rate ~80 times faster than in the solar reactor and an associated average rate of 2.2 ± 0.2 ml min^{-1} g^{-1} of ceria; CO_2 and H_2O dissociation reactions were about two and four times faster (although the reactant partial pressures, temperatures, and initial extents of reduction differ slightly between the differential and solar reactor), with rates of 5.1 ± 0.4 and 5.3 ± 0.4 ml min^{-1} g^{-1} of ceria, respectively. These rates support the proposition that oxygen evolution kinetics in the solar reactor are limited predominantly by the heating rate.

The solar-to-fuel energy conversion efficiency is defined as

$$\eta = \frac{r_{fuel}\Delta H_{fuel}}{P_{solar} + r_{inert}E_{inert}} \quad (4)$$

where r_{fuel} is the molar fuel production rate, ΔH_{fuel} is the higher heating value of the fuel, P_{solar} is the incident solar radiation power, r_{inert} is the flow rate of the inert gas during oxygen evolution, and E_{inert} is the energy required to separate the inert sweep gas from air (usually N_2; Ar was used in this work entirely for reasons of experimental convenience). Based on the experimental data, the peak instantaneous efficiencies for CO_2 and H_2O dissociations reached 0.8% and 0.7%, respectively [for detailed calculation procedures, see (*25*)]. No heat recuperation strategy was used. Upon averaging the efficiencies over the time required to produce 80% of the fuel, the efficiencies become 0.4% (for both CO_2 and H_2O dissociations). These experimentally measured efficiencies reflect the cycle irreversibilities resulting from intrinsic material properties as well as solar reactor design and operation. An energy-balance analysis (*25*) reveals that 50% of the energy loss resulted from heat conduction through the reactor wall and 41% resulted from reradiation through the aperture. The former energy penalty can be dramatically reduced by improving thermal insulation and by scaling up to increase the volume-to-area ratio. The latter can be minimized by augmenting the solar flux such that the aperture size can be reduced. Decreasing heat loss also has the added benefit of increasing the temperature ramp rate. As shown in the earlier comparison of the oxygen evolution kinetics under slow and rapid heating rates, the oxygen evolution kinetics and conversion efficiency are closely coupled to the rates at which the active ceria materials can be heated and cooled.

Beyond efficiency, material stability is an essential criterion for a viable thermochemical process. With use of the differential reactor system, which enables rapid access to multiple cycles, 500 cycles of water dissociation were performed without interruption. The results (Fig. 4), reported in part in an earlier work (*21*), indicate that, after an initial stabilization period of ~100 cycles, both the oxygen and hydrogen evolution rates remain essentially constant for a subsequent 400 cycles. Scanning electron microscopy examination of samples of porous ceria that underwent heat treatment under similar conditions (fig. S3) revealed that the decrease in reaction rate is accompanied by an increase in particle size. The morphology stabilized after 24 hours of heat treatment at 1500°C, much as the fuel production rate stabilized after an initial period. That ceria can be cycled between two oxidation states without substantial loss of activity can be attributed to its sufficiently large change in oxygen nonstoichiometry at moderate homologous temperatures (<0.6 × T_m).

In sum, the feasibility of a solar-driven thermochemical cycle for dissociating H_2O and CO_2 using nonstoichiometric ceria has been demonstrated in terms of materials, reaction rates, cyclability, reactor technology, and energy conversion efficiency. Essential to this demonstration is a simple and scalable reactor design using porous ceria directly exposed to concentrated solar radiation that enables high-temperature heat transfer to the reaction sites, as required for performing both steps of the cycle. The solar-to-fuel energy conversion efficiency obtained in this work for CO_2 dissociation is about two orders of magnitude greater than that observed with state-of-the-art photocatalytic approaches (*3*, *9*).The gravimetric hydrogen production rate exceeds that of other solar-driven thermochemical processes by more than an order of magnitude (*27*, *28*). Both the efficiency and the cycling rates in the reactor were limited largely by thermal losses, resulting from conductive and radiative heat transfer. A thermodynamic analysis of efficiency based solely on the material properties of CeO_2 indicates that values in the range of 16 to 19% are attainable, even in the absence of sensible heat recovery (*21*). Thus, with reactor optimization and system integration substantial increases in both efficiency and fuel production rates are anticipated. The material stability, showing stable fuel production over 500 thermochemical cycles, is already suitable for realistic applications. Furthermore, the abundance of cerium, which is comparable to that of copper (*29*), is such that the approach is applicable at scales relevant to global energy consumption (*21*).

References and Notes

1. N. S. Lewis, D. G. Nocera, *Proc. Natl. Acad. Sci. U.S.A.* **103**, 15729 (2006).
2. H. Takeda, K. Koike, H. Inoue, O. Ishitani, *J. Am. Chem. Soc.* **130**, 2023 (2008).
3. S. C. Roy, O. K. Varghese, M. Paulose, C. A. Grimes, *ACS Nano* **4**, 1259 (2010).
4. Y. Hori, K. Kikuchi, S. Suzuki, *Chem. Lett.* **14**, 1695 (1985).
5. V. P. Indrakanti, J. D. Kubicki, H. H. Schobert, *Energy Environ. Sci.* **2**, 745 (2009).
6. T. Inoue, A. Fujishima, S. Konishi, K. Honda, *Nature* **277**, 637 (1979).
7. O. Khaselev, J. A. Turner, *Science* **280**, 425 (1998).
8. K. R. Thampi, J. Kiwi, M. Gratzel, *Nature* **327**, 506 (1987).
9. O. K. Varghese, M. Paulose, T. J. Latempa, C. A. Grimes, *Nano Lett.* **9**, 731 (2009).
10. E. A. Fletcher, *J. Sol. Energy Trans. Am. Soc. Mech. Eng.* **123**, 63 (2001).
11. A. Steinfeld, *Sol. Energy* **78**, 603 (2005).
12. L. O. Schunk, A. Steinfeld, *AIChE J.* **55**, 1497 (2009).
13. L. O. Schunk, W. Lipinski, A. Steinfeld, *Chem. Eng. J.* **150**, 502 (2009).
14. T. Kodama, N. Gokon, *Chem. Rev.* **107**, 4048 (2007).
15. M. Chambon, S. Abanades, G. Flamant, *Chem. Eng. Sci.* **65**, 3671 (2010).

Downloaded from www.sciencemag.org on January 3, 2011

16. D. Gstoehl, A. Brambilla, L. O. Schunk, A. Steinfeld, *J. Mater. Sci.* **43**, 4729 (2008).
17. J. E. Miller *et al.*, *J. Mater. Sci.* **43**, 4714 (2008).
18. C. Perkins, A. W. Weimer, *AIChE J.* **55**, 286 (2009).
19. P. Singh, M. S. Hegde, *Chem. Mater.* **22**, 762 (2010).
20. W. C. Chueh, S. M. Haile, *ChemSusChem* **2**, 735 (2009).
21. W. C. Chueh, S. M. Haile, *Philos. Trans. R. Soc. London Ser. A* **368**, 3269 (2010).
22. S. M. Haile, W. C. Chueh, U.S. Patent application 20,090,107,044 (2009).
23. S. Abanades *et al.*, *J. Mater. Sci.* **45**, 4163 (2010).
24. H. Kaneko *et al.*, *Energy* **32**, 656 (2007).
25. Materials and methods are detailed in supporting material at *Science* Online.
26. C. Li, L. Minh, T. C. Brown, *J. Catal.* **178**, 275 (1998).
27. M. Roeb *et al.*, *Int. J. Hydrogen Energy* **34**, 4537 (2009).
28. Fuel production rate is compared with other thermochemical processes by normalizing the average fuel production rate (as defined in the text) by the mass of the material, including inactive support used to prevent material sintering. The rate for oxygen evolution is not included.
29. G. B. Haxel, J. B. Hedrick, G. J. Orris, "Rare earth elements—Critical resources for high technology" (U.S. Geological Survey Fact Sheet 087-02, Reston, VA, 2002).
30. This work was funded in part by NSF (CBET-0829114), the Initiative for Renewable Energy and the Environment (under subcontract from the University of Minnesota), and the Swiss National Science Foundation (contract no. 200021-126512). Additional travel support was provided by the International Materials Institutes program of NSF under award no. DMR 08-43934. We thank the technical staff of the Solar Technology Laboratory of the Paul Scherrer Institute for supporting the experimental activities at the High-Flux Solar Simulator. W.C.C. designed the experiments, and C.F. designed the solar reactor. Samples were prepared by M.A. and D.S. W.C.C, C.F., P.F., and D.S. executed the experiments. S.M.H. and A.S. supervised the project.

Supporting Online Material

www.sciencemag.org/cgi/content/full/330/6012/1797/DC1
Materials and Methods
Figs. S1 to S3

15 September 2010; accepted 23 November 2010
10.1126/science.1197834

Spin Hall Effect Transistor

Jörg Wunderlich,[1,2*†] Byong-Guk Park,[1*] Andrew C. Irvine,[3*] Liviu P. Zârbo,[2] Eva Rozkotová,[4] Petr Nemec,[4] Vít Novák,[2] Jairo Sinova,[5,2] Tomás Jungwirth[2,6]

The field of semiconductor spintronics explores spin-related quantum relativistic phenomena in solid-state systems. Spin transistors and spin Hall effects have been two separate leading directions of research in this field. We have combined the two directions by realizing an all-semiconductor spin Hall effect transistor. The device uses diffusive transport and operates without electrical current in the active part of the transistor. We demonstrate a spin AND logic function in a semiconductor channel with two gates. Our study shows the utility of the spin Hall effect in a microelectronic device geometry, realizes the spin transistor with electrical detection directly along the gated semiconductor channel, and provides an experimental tool for exploring spin Hall and spin precession phenomena in an electrically tunable semiconductor layer.

Two major themes in semiconductor spintronics research, the spin transistors and the spin Hall effects, have followed distinct and independent scientific paths (*1*, *2*). In the transistor case, the target device concept of a ferromagnetic spin injector and detector connected by a semiconductor channel was established from the outset by Datta and Das (*3*). The ensuing research has focused on the fundamental physical problems related to the resistance mismatch between the transistor's components and to the spin manipulation in the semiconductor via spin-orbit coupling effects (*4*–*15*). By contrast, in the spin Hall effect case, much of the related intriguing quantum-relativistic physics (*16*–*19*) has been established before the first experimental observations (*20*, *21*), but the field is still striving to turn the phenomenon into a concrete device functionality. We demonstrate the applicability of the spin Hall effect in a new type of spin transistor.

The active semiconductor channel in our devices is a two-dimensional electron gas (2DEG) in which the spin-orbit coupling induced spin precession is controlled by external gate electrodes and detection is provided by transverse spin Hall

[1]Hitachi Cambridge Laboratory, Cambridge CB3 0HE, UK. [2]Institute of Physics ASCR, v.v.i., Cukrovarnická 10, 162 53 Praha 6, Czech Republic. [3]Microelectronics Research Centre, Cavendish Laboratory, University of Cambridge, CB3 0HE, UK. [4]Faculty of Mathematics and Physics, Charles University in Prague, Ke Karlovu 3, 121 16 Prague 2, Czech Republic. [5]Department of Physics, Texas A&M University, College Station, TX 77843–4242, USA. [6]School of Physics and Astronomy, University of Nottingham, Nottingham NG7 2RD, UK.

*These authors contributed equally to this work.
†To whom correspondence should be addressed. E-mail: jw526@cam.ac.uk

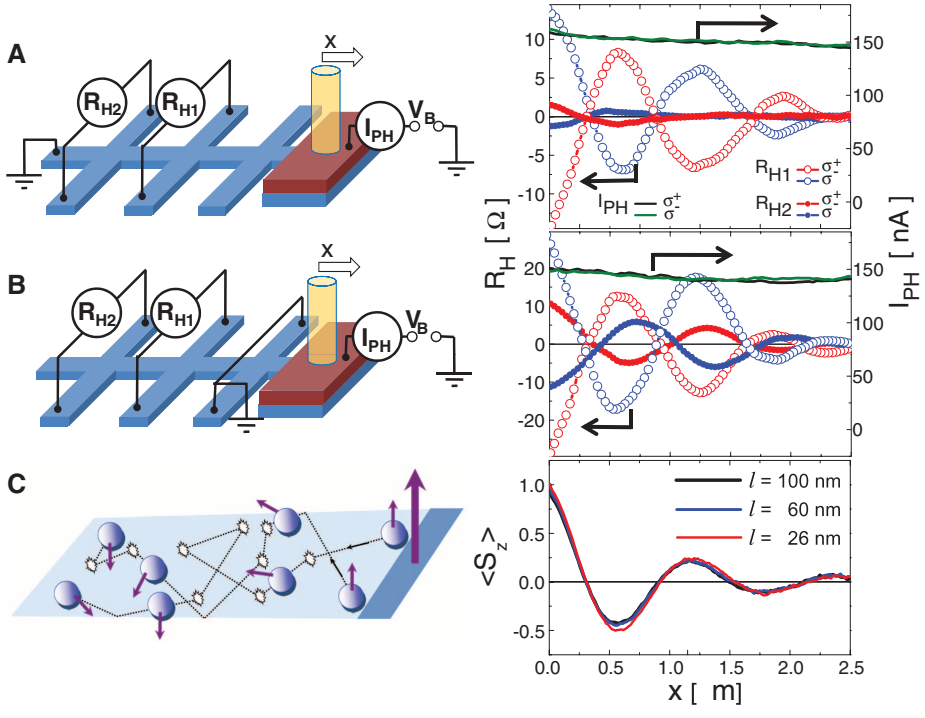

Fig. 1. (**A**) Schematics of the measurement setup with optically injected spin-polarized electrical current propagating through the Hall bar and corresponding experimental Hall effect signals at crosses H1 and H2. The Hall resistances, $R_H = V_H/I_{PH}$, for the two opposite helicities of the incident light are plotted as a function of the focused (~1 μm) light spot position, i.e., of the position of the injection point. Increasing x corresponds to shifting the spot further away from the Hall detectors. (The focused laser beam is indicated by the yellow cylinder in the schematics.) The optical current I_{PH} is independent of the helicity of the incident light and varies only weakly with the light spot position. The applied bias voltage $V_B = -15$ V, the laser intensity is 1000 W/cm^2, and the laser wavelength is 870 nm. (**B**) Same as (A) for measurement geometry in which electrical current is closed before the first detecting Hall cross H1. (**C**) Schematics of the diffusive transport of injected spin-polarized electrons and Monte-Carlo simulations of the out-of-plane component of the spin of injected electrons averaged over the 1-μm bar cross section assuming Rashba field $\alpha = 5.5$ meV Å, Dresselhaus field $\beta = -24$ meV Å, and different values of the mean free path l.

Downloaded from www.sciencemag.org on January 3, 2011